ISPRS Journal of Photogrammetry and Remote Sensing 102 (2015) 148–160

Contents lists available at ScienceDirect

ISPRS Journal of Photogrammetry and Remote Sensing

journal homepage: www.elsevier.com/locate/isprsjprs

Spatio-temporal prediction of leaf area index of rubber plantation using HJ-1A/1B CCD images and recurrent neural network

Bangqian Chen [a], Zhixiang Wu [a], Jikun Wang [a], Jinwei Dong [b], Liming Guan [a], Junming Chen [a], Kai Yang [c], Guishui Xie [a,*]

[a] Danzhou Investigation & Experiment Station of Tropical Cops, Ministry of Agriculture, Rubber Research Institute, Chinese Academy of Tropical Agricultural Sciences (CATAS), Danzhou 571737, PR China
[b] Department of Microbiology and Plant Biology, Center for Spatial Analysis, University of Oklahoma, Norman, OK 73019, USA
[c] Department of Corporate Affairs, CFPA Microfinance, China Foundation for Poverty Alleviation, Beijing 10086, PR China

ARTICLE INFO

Article history:
Received 24 September 2013
Received in revised form 7 October 2014
Accepted 5 December 2014

Keywords:
Leaf area index
Rubber plantation
HJ-1A/1B CCD
Recurrent neural network
NARX
Hainan Island

ABSTRACT

Rubber (*Hevea brasiliensis*) plantations are one of the most important economic forest in tropical area. Retrieving leaf area index (LAI) and its dynamics by remote sensing is of great significance in ecological study and production management, such as yield prediction and post-hurricane damage evaluation. Thirteen HJ-1A/1B CCD images, which possess the spatial advantage of Landsat TM/ETM+ and 2-days temporal resolution of MODIS, were introduced to predict the spatial–temporal LAI of rubber plantation on Hainan Island by Nonlinear AutoRegressive networks with eXogenous inputs (NARX) model. Monthly measured LAIs at 30 stands by LAI-2000 between 2012 and 2013 were used to explore the LAI dynamics and their relationship with spectral bands and seven vegetation indices, and to develop and validate model. The NARX model, which was built base on input variables of day of year (DOY), four spectral bands and weight difference vegetation index (WDVI), possessed good accuracies during the model building for the data set of training ($N = 202$, $R^2 = 0.98$, $RMSE = 0.13$), validation ($N = 43$, $R^2 = 0.93$, $RMSE = 0.24$) and testing ($N = 43$, $R^2 = 0.87$, $RMSE = 0.31$), respectively. The model performed well during field validation ($N = 24$, $R^2 = 0.88$, $RMSE = 0.24$) and most of its mapping results showed better agreement ($R^2 = 0.54$–0.58, $RMSE = 0.47$–0.71) with the field data than the results of corresponding stepwise regression models ($R^2 = 0.43$–0.51, $RMSE = 0.52$–0.82). Besides, the LAI statistical values from the spatio-temporal LAI maps and their dynamics, which increased dramatically from late March (2.36 ± 0.59) to early May (3.22 ± 0.64) and then gradually slow down until reached the maximum value in early October (4.21 ± 0.87), were quite consistent with the statistical results of the field data. The study demonstrates the feasibility and reliability of retrieving spatio-temporal LAI of rubber plantations by an artificial neural network (ANN) approach, and provides some insight on the application of HJ-1A/1B CCD images, and data and methods for productivity study of rubber plantation in future.

1. Introduction

Rubber trees *(Hevea brasiliensis)*, widely planted hardwood genus in tropical areas, are important suppliers of natural rubber and wood. Cultivation of rubber trees is of great economic significance and has a profound effect on the local ecosystems. For example, Hainan Island, the largest rubber cultivation base in China, grew about 4.4×10^5 ha of rubber trees in 2010, occupying 13.8% of the total land area of the island and forming the largest artificial ecosystem there (Chen et al., 2007; Ju-sheng and Rusong, 2003; Chen J. et al., 2010; Mo, 2010). Rubber trees are generally planted 5–8 m apart in rows and 3–4 m in spacing and have a rotation length of typically 30–40 years. They have an immature stage (non-productivity) of about 7 years. Great structural changes of the canopy of the trees not only occur during their life cycle, but also in each season because rubber trees present deciduous behaviors in northern parts of the tropics. Precise temporal and spatial estimation of leaf area index (LAI), which is typically defined as one half the total leaf area per unit ground surface area (Jonckheere et al., 2004), is very important for scientists in their understanding and modeling gas-vegetation exchange processes

* Corresponding author. Tel.: +86 0898 23306385.
E-mail addresses: chbq40@163.com (B. Chen), xie23300459@sina.com (G. Xie).

http://dx.doi.org/10.1016/j.isprsjprs.2014.12.011
0924-2716/© 2014 Published by Elsevier B.V. on behalf of International Society for Photogrammetry and Remote Sensing, Inc. (ISPRS).

such as photosynthesis, evaporation and transpiration, rainfall interception, carbon flux and nutrient cycle (Chen et al., 2004; Chen and Cihlar, 1996; Jensen et al., 2011; Maass et al., 1995; Soudani et al., 2006; Zheng and Moskal, 2009), and is also critical for production management.

Previous studies have incorporated LAI as important parameters for modeling the photosynthesis, respiration and dry matter accumulation of rubber trees (Hu et al., 1982; Xie, 2009; Xie et al., 2010). The established models can be further used for research on productive potential and yield prediction. In addition, LAI has been found to be positively correlated with dry rubber production ($R^2 = 0.71$), and to be used to manage tapping intensity in the field for higher rubber yield (Righi and Bernardes, 2008). The tapping intensity is particularly important in production management. Tapping with too high frequency would endanger the survival of rubber trees, while too low frequency is not good for gaining high yield of latex. Therefore, farmers might directly benefit from adjusting the tapping intensity scientifically by monitoring the LAI over a large area.

LAI may also serve as an important parameter in assessment of post-hurricane (or typhoon, tropical cyclone) damage to rubber plantations, which is particular important in China. About half of the plantations are in Hainan and Guangdong provinces frequently struck by hurricanes (Yu et al., 2006; Zhang K. et al., 2010)). As rubber tree is a labor-intensive crop with high output value, accurate post-hurricane damage assessment is helpful for farmers to obtain reasonable compensation from both the government and the insurance company (Fu and Zhang, 2010; Zhang, 2011). The canopy size and its density level are key parameters in evaluating post-hurricane damage since they directly determine the wind pressure of rubber plantations (He and Huang, 1987). The modification of canopy during the hurricane may be related with the fundamental biophysical parameter of LAI, and could be identified from moderate or high spatial resolution images. For example, Aosier et al. (2007) found LAI to be an important index for extraction of fallen trees from Advanced Spaceborne Thermal Emission and Reflection Radiometer (ASTER) images.

However, the LAI dynamics is still unknown for rubber plantations, either on a site-specific or regional scale. The emergence of remote sensing has significantly improved the LAI estimation on a large scale (Fassnacht et al., 1997; Zheng and Moskal, 2009), and numerous studies have been performed to retrieve the LAI of coniferous forests (Berterretche et al., 2005; Chen et al., 2004; Sprintsin et al., 2011; Tian et al., 2007), broadleaf forests (le Maire et al., 2011), croplands (González-Sanpedro et al., 2008) and mixtures of vegetation types (Fang and Liang, 2005; Gray and Song, 2012; Jensen et al., 2011; Soudani et al., 2006). However, few studies have been conducted to deal with rubber trees. One of the main problems of applying optical remote sensing technology to rubber plantations is the constant presence of clouds and cloud shadows in the tropical area (Wang et al., 1999). Medium- and high-resolution satellites typically have longer revisit intervals of about two weeks or longer, making it very difficult to acquire an image at a fixed time and in a specific region from a specific satellite. The MODIS can re-visit the same place once two days, but it is difficult to use it to monitor the changes of the small and medium-sized rubber plantations due to its relatively low spatial resolution (Soudani et al., 2006). In addition, it is difficult to use multi-source satellite data because of the differences in the spectral and spatial characteristics of the sensors (Soudani et al., 2006).

China launched two small environmental satellites named HJ-1A and HJ-1B (HJ-1A/1B for short hereinafter) on September 6, 2008. They are sun-synchronous circular orbit satellites with an orbital altitude of 649 km. The Wide View CCD Cameras (WVC) instrument with dual camera configuration onboard HJ-1A/1B have four bands including blue (0.43–0.52 μm), green (0.52–0.60 μm), red (0.63–0.69 μm), and near-infrared (NIR, 0.76–0.90 μm) spectra, with the same the spectral ranges as the first four bands of the Landsat TM/ETM+. The CCD imagery is 360 km in swath width and possesses the advantages of both Landsat and MODIS images, with 30 m spatial resolution and 2-day revisit interval period, by constellation of the two satellites (Lu et al., 2011). It has been widely used in estimating the LAI of winter wheat (Chen X. et al., 2010; Zhang et al., 2011; Hu et al., 2012), prairie (Sun et al., 2011), forest (Zhu et al., 2011), and rice (Li et al., 2011; Zhang J. et al., 2010).).

This study was to explore the feasibility of using multi-temporal HJ-1A/1B CCD images to predict spatio-temoral LAI by the artificial neural network (ANN) approach. The ANN is theoretically capable of handling the non-normality, nonlinearity and collinearity data not dealt by statistical methods, and is simpler than the radiative transfer equation based physical models (Houborg et al., 2007; Walthall et al., 2004), and has been widely used for multispectral and multi-temporal digital image classification (Li and Fox, 2011; Murnion, 1996; Shupe and Marsh, 2004), biomass and forest stand age extraction (Chen et al., 2012; Jensen et al., 1999; Muukkonen and Heiskanen, 2005), and LAI estimation (Bacour et al., 2006; Fang and Liang, 2003, 2005; Walthall et al., 2004; Linna et al., 2009). Since the LAI of rubber plantation should be nonlinear continuous time series if without serve natural disaster disturbance, a commonly used time-serials ANN model, the Nonlinear AutoRegressive networks with eXogenous inputs (NARX), was selected in this study (Menezes and Barreto, 2008; Pisoni et al., 2009; Siegelmann et al., 1997). The NARX model has been used to predict the spatio-temporal change of snow cover (Sauter et al., 2010) and time-serials LAI (Chai et al., 2012) with MODIS data, and works very promising not only in single-pixel value retrieval but also in time-serials prediction.

2. Materials and methods

2.1. Study area

The experimental farm (19°30′N, 109°29′E) of Chinese Academy of Tropical Agricultural Sciences (CATAS) is located in Danzhou city, the largest rubber production base of Hainan Island, China (Fig. 1). The topography of the farm is characterized by hilly plateau with elevations of 130–200 m above the sea level. The sunny and tropical weather with monsoons here are favorable for agricultural development. The annual precipitation is about 1815 mm. The rainy season (May–October) accounts for over 84% of the annual total rainfall and witnesses frequent hurricane of various scales. The solar radiation is strong in this area with annual average sunshine of more than 2000 h and an annual average temperature of 23.1 °C. The farm occupies 3299 ha of cropland, of which 1529 ha are rubber plantations.

A total of 30 rubber stands with areas ranging from 1.16 to 14.48 ha were randomly sampled. Eight of the 30 stands were used for long-term monitoring by Danzhou Investigation & Experimental Station of Tropical Crop, Ministry of Agriculture, P.R. China. Four clones including CATAS7-33-97, PR107, RRIM600 and CATAS7-20-59 were selected. The stand age was 16.2 years by average, ranging from 7 to 30 years. There were 7, 8, 7, 3 and 5 stands within the age groups of <10, 11–15, 16–20, 21–25, >25 years, respectively. The boundaries of sampling stands (stand digital map for short hereinafter) were delineated on a 5.8 m multi-spectral image derived from ZY3 satellite (Table 1). The ZY3 satellite was launched on January 9, 2012 and was the China's first civilian high-resolution stereo mapping satellite (http://www.cresda.com). The stand digital map was stored as shapefile format. The understory plant species are mainly *Piper sarmentosum Roxb.*, *Ottochloa nodosa (Kunth)*

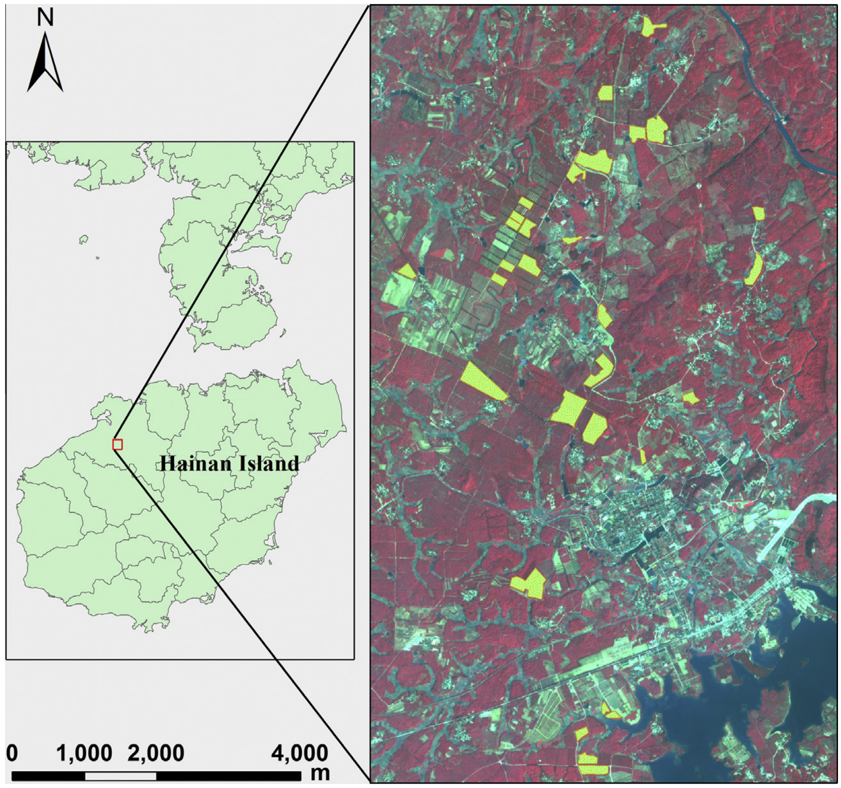

Fig. 1. The location of study area and 30 rubber stands within the CATAS experimental farm, Danzhou, Hainan Island, China. The background was 5.8 m spatial resolution ZY3 image acquired on March 23, 2012 and was shown in band combination of R(4) G(3) B(2) with 2% linear stretch. The green patches were the exact location of the sampling stands. (For interpretation of the references to colour in this figure legend, the reader is referred to the web version of this article.)

Table 1
Satellite data set description, including path, row, acquisition date and time, solar elevation and azimuth angle (degree).

No.	Satellite	Sensor	Path	Row	Date	DOY	Time	Sun elevation	Sun azimuth
1	HJ-1B	CCD2	5	92	2012/03/23	82	11:04:23	58.00	305.57
2	ZY3	MUX	6	175	2012/03/23	82	11:20:25	61.74	307.99
3	HJ-1A	CCD1	2	92	2012/04/24	114	11:08:00	67.25	286.47
4	HJ-1A	CCD2	3	96	2012/05/01	121	10:52:48	64.63	272.95
5	HJ-1B	CCD2	4	92	2012/05/03	123	11:00:05	64.34	277.98
6	HJ-1A	CCD1	3	92	2012/05/09	129	11:09:02	68.40	274.95
7	HJ-1B	CCD2	2	96	2012/05/14	134	10:55:04	64.67	264.63
8	HJ-1A	CCD2	2	96	2012/07/11	192	10:50:16	64.13	256.52
9	HJ-1B	CCD2	3	96	2012/07/13	194	10:52:56	63.84	257.25
10	HJ-1A	CCD2	4	92	2012/07/15	196	10:55:47	64.97	264.07
11	HJ-1B	CCD1	1	92	2012/10/04	277	10:55:04	54.87	312.55
12	HJ-1A	CCD2	3	96	2012/10/13	286	10:46:59	51.69	310.02
13	HJ-1B	CCD2	5	92	2012/11/22	326	10:50:53	41.90	321.33
14	HJ-1A	CCD2	2	96	2012/12/01	334	10:41:48	40.71	322.86

Dandy, *Callipterisesculenta* (*Retz.*) J. *Sm. ex Moore et Houlst*., *Panicum brevifolium* L., *Axonopus compressus (Sw.) Beauv*., and *Lophatherum gracile Brongn*.

2.2. Field data and satellite images

2.2.1. Field-LAI measurements

The Plant Canopy Analyzer (PCA) LAI-2000 (LICOR Inc., Lincoln, NE, USA) was used to measure LAI. The LAI-2000 measured the gap fraction $P(\theta)$ in five zenith angles (θ) with midpoints of 7°, 23°, 38°, 53° and 67° and calculated LAI based on Miller's theorem. Actually, the LAI obtained from the gap fraction measurements was effective LAI (Chen and Cihlar, 1996), but hereinafter was referred as LAI for short. Among the 30 stands, the data of 24 stands were used to explore the general pattern of seasonal LAI and to build NARX model (hereinafter referred as model-building stands), and the data of the rest six stands were used for model validation (hereinafter referred as model-validation stands). The measurement for the model building stands was started in March 2012 and for the validation stands was begun in August 2012. All the measurements were conducted around 25th of every month and were ended in February 2013.

Improving the accuracy of ground-based data is critical to the advancement of remote sensing application (Chen and Cihlar, 1996). Therefore, all measurements were taken under uniform or near uniform clear diffuse skies at low solar elevation to prevent the effect of direct sunlight on the sensor and to reduce light scattering effect (e.g., for less than two hours after sunrise and before sunset for sunny days). To avoid direct sunlight on the sensor, the above-canopy (A) and below-canopy (B) readings were made in the opposite direction of the sun using a view gap of 45° in the azimuthal plane. For each stand, two A reference samples with at least 8 readings were quickly measured before and after the B readings at a closed (300 m or less) open area, which was sufficiently large so that no potential field view would be obstructed (LI-COR, 1992). Based on the stand area, 24–36 B readings were taken along the row diagonals of each stand by the same LAI-2000 instrument. The intervals between two B readings ranged from 5 to 10 m and at least two transects were performed to obtain a representative measurement. All B readings were collected at a minimum distance from the edges, about two times the maximum tree height to avoid border effect.

2.2.2. Satellite Images

Thirteen successive HJ-1A/1B CCD images and one ZY3 MUX multispectral image were obtained from China Centre for Resources Satellite Data and Application (CRESDA). Images obtained in February were not used because most rubber trees shed their leaves. Table 1 lists the image acquisition and the illumination geometries. All the images were acquired around 11:00 AM, but the angles of sun azimuth and zenith changed with seasons. The different values of path and row indicated that the orbit of HJ-1A/1B had a certain offset. All the CCD images were treated with radiometric and geometric correction (level 2).

2.3. Data processing

2.3.1. Field-LAI processing

Computation of LAI was done using LAI-COR FV2200, which allowed manipulation of LAI-2200 and LAI-2000 data (LI-COR, 2012). Although we tried to make sure all the measurements were under ideal conditions, some data processing methods were still used to reduce possible errors caused by the changing of the environment. For each B reading of each stand, an A reading was determined by time-based linear interpolation between two associated A samples. The assumption of linear variation of above-canopy radiation with time at low solar angle elevation was verified for a short time (less than 20 min) delay between two samples (Soudani et al., 2006). The mean values of each A reference sample were calculated and used to interpolate an A reading for each B reading. Previous studies indicated that discarding two lowest rings (47–58° and 61–74°) of LAI-2000 could improve LAI estimation for broadleaf species (Olthof and King, 2000; Soudani et al., 2006; Welles and Norman, 1991). Therefore, only the three upper rings were used to compute LAI for the broadleaf rubber trees.

2.3.2. Satellite images pre-processing

The HJ-1B CCD2 image acquired on March 23, 2012 was re-projected into a UTM zone 49N and was geometrically corrected by using 25 ground control points gathered throughout the image utilizing features such as small ponds and road intersections. Nearest neighbor resampling was used in all geometrical transformations to minimize the statistical properties change of the data sets. A second order of polynomial transformation equation was used to re-project the images with a root mean square error (RMSE) of less than 0.5 pixels. The corrected image was further used as reference image to register the rest images by the automatic registration utility of ENVI. The digital number (DN) values were converted to at-sensor spectral radiance, L_{sat} ($\mathrm{Wm^{-2}\,sr^{-1}\,\mu m^{-1}}$), by radiometric calibration, and were then converted into Top-Of-Atmosphere (TOA) reflectance. The radiometric calibration of HJ-1A/1B CCD images was made by using Eq. (1).

$$L_{sat} = \frac{\mathrm{DN}}{G} + L_0 \tag{1}$$

where G ($\mathrm{W^{-1}m^2\,sr\,\mu m}$) was the calibration factor and L_0 ($\mathrm{Wm^{-2}\,sr^{-1}\,\mu m^{-1}}$) was the calibration offset. The G and L_0 were restored in the corresponding header file and were presented in Table 2.

The conversion of at-sensor spectral radiance to exoatmospheric TOA reflectance was performed by using Eq. (2)

$$\rho = \frac{\pi L D^2}{E_{sun}\cos\theta_s} \tag{2}$$

where the L was at-sensor radiance, D was the Earth-Sun distance in astronomical units, E_{sun} was the mean solar exo-atmospheric irradiance, and θ was the solar zenith angle. The D was varied with the Day-Of-Year (DOY) and was retrieved from Chander et al. (2009) according to the DOY of the image acquisition date. For HJ-1A/1B CCD images, the E_{sun} was presented in Table 3 (Zhu et al., 2011). Since there was no well-accepted atmospheric correction model available for HJ-1A/1B satellites, no atmospheric correction was performed on HJ-1A/1B CCD images.

For ZY3 images, no geometric correction was performed because its positioning precision was high. The radiometric calibration was made by using Eq. (3).

$$L_{sat} = G \cdot \mathrm{DN} \tag{3}$$

where the gain G ($\mathrm{W^{-1}m^2\,sr\,\mu m}$) was set at 0.2525, 0.2253, 0.1791 and 0.1942 for the spectral band of blue, green, red and NIR, respectively (http://www.cresda.com). The conversion of spectral radiance to exoatmospheric TOA reflectance was not performed because E_{sun} in Eq. (2) was not obtained.

2.3.3. Vegetation indices computation

Seven vegetation indices (VIs), which were frequently used for LAI estimation, including Normalized Difference Vegetation Index (NDVI), Simple Ratio (SR), Soil Adjusted Vegetation Index (SAVI), second version of SAVI (SAVI2), Transformed SAVI (TSAVI), Weighted Difference Vegetation Index (WDVI) and Enhanced Vegetation Index (EVI), were computed using the following equations (Broge and Leblanc, 2000; Liang and Liang, 2003; Turner et al., 1999).

$$\mathrm{NDVI} = \frac{\rho_{NIR} - \rho_{red}}{\rho_{NIR} + \rho_{red}} \tag{4}$$

Table 2
Coefficients used for radiometric calibration of HJ-1A/1B CCD images.

Satellite	Sensor		$B1$ (0.43–0.52 μm)	$B2$ (0.52–0.60 μm)	$B3$ (0.63–0.69 μm)	$B4$ (0.76–0.90 μm)
HJ-1A	CCD1	G	0.7696	0.7815	1.0914	1.0281
		L_0	7.3250	6.0737	3.6123	1.9028
HJ-1A	CCD2	G	0.7435	0.7379	1.0899	1.0852
		L_0	4.6344	4.0982	3.7360	0.7385
HJ-1B	CCD1	G	0.7060	0.6960	1.0082	1.0068
		L_0	3.0089	4.4487	3.2144	2.5609
HJ-1B	CCD2	G	0.8042	0.7822	1.0556	0.9237
		L_0	2.2219	4.0683	5.2537	6.3497

Table 3
Mean solar exo-atmoshperic irradiance (E_{sun}, $Wm^{-2}\ \mu m^{-1}$) used for TOA reflectance calibration of HJ-1A/1B CCD images.

Satellite	Sensor	*B*1	*B*2	*B*3	*B*4
HJ-1A	CCD1	1914.324	1825.419	1542.664	1073.826
	CCD2	1929.810	1831.144	1549.824	1078.317
HJ-1B	CCD1	1902.188	2833.626	1566.714	1077.085
	CCD2	1922.897	1823.985	1553.201	1074.544

$$\mathrm{SR} = \frac{\rho_{\mathrm{NIR}}}{\rho_{\mathrm{red}}} \tag{5}$$

$$\mathrm{SAVI} = \frac{\rho_{\mathrm{NIR}} - \rho_{\mathrm{red}}}{\rho_{\mathrm{NIR}} + \rho_{\mathrm{red}} + L}(1 + L) \tag{6}$$

$$\mathrm{SAVI2} = \frac{\rho_{\mathrm{NIR}}}{\rho_{\mathrm{red}} + \frac{b}{\gamma}} \tag{7}$$

$$\mathrm{TSAVI} = \frac{\gamma(\rho_{\mathrm{NIR}} - \gamma\rho_{\mathrm{red}} - b)}{\gamma\rho_{\mathrm{NIR}} + \rho_{\mathrm{red}} + \gamma b + X(1 + \gamma^2)} \tag{8}$$

$$\mathrm{WDVI} = \rho_{\mathrm{NIR}} - \gamma\rho_{\mathrm{red}} \tag{9}$$

$$\mathrm{EVI} = 2.5 \times \frac{\rho_{\mathrm{NIR}} - \rho_{\mathrm{red}}}{\rho_{\mathrm{NIR}} + 6 \times \rho_{\mathrm{red}} - 7.5 \times \rho_{\mathrm{blue}} + 1} \tag{10}$$

where ρ_{blue}, ρ_{red}, and ρ_{NIR} were the reflectance values of blue, red, and NIR spectral bands of HJ-1A/1B CCD, respectively. The L was a canopy background adjustment factor set at 0.5 (Soudani et al., 2006), and γ and b were the slope and intercept, respectively, of the soil line. X was the adjustment factor to minimize the soil noise set at 0.08 (Liang and Liang, 2003). The slope and intercept of soil line were determined from the red-NIR spectral space of each image following the method published by Fang and Liang (2003). The VIs layers and four spectral bands were stacked for subsequent analysis.

2.3.4. Spectral feature of rubber stand extraction

The mean value of each stand, instead of the mean value of 3×3 pixels window centered at each sampling point (Chen and Cihlar, 1996; Foody et al., 2001), was extracted from each image. The mean stand value was used due mainly to the following considerations. Firstly, the mean value could represent the reflectance level of the whole stand because rubber trees were simultaneously transplanted in each stand and were managed with same measures during their life cycle. Secondly, a 3×3 pixels window in HJ-1A/1B CCD image meant that the stand contained at least one square area of 1 ha. Therefore, the mean value had stronger adaptability in dealing with small or thin stands that did not meet this requirement.

The stand digital map was used to create regions of interest (ROIs), and further used for extracting pixel values. Since the boundary pixels might be contaminated by roads and windbreak forest, the pixels of the first and last lines, the head and tail pixels of the remaining lines in each ROI were removed (Chen et al., 2012). Some inner-stand outlier pixels, which came from extremely ruined spots such as continuous break of trunks or missing of trees due to the frequent hurricane disturbance, should also be removed. Ideally, pixels from highly homogeneous rubber stands might have similar values in each spectral band, while pixels from the extremely ruined spots could exhibit quite different values. Therefore, outlier pixels could be identified in a sorted pixel order. In this study, only percentile values of pixels in each ROI that in four spectral bands all are within (0.05, 0.95) were used. The filter of boundary pixels or inner-stand outlier, however, was not performed for small stands if the filtered pixels were smaller than a threshold value (4 was used here). All the processes were finished by an Interactive Data Language (IDL) and ENVI based programs (http://www.exelisvis.com/).

2.3.5. Field data processing and regression analysis

Statistical analysis was performed on the field LAI of model-building stands and the mean LAI of these stands was used to explore the general pattern of seasonal LAI of rubber plantation. For each image, a corresponding field LAI was determined by linear interpolation from the two closest field data based on the DOY of the image acquisition date and field campaign. The interpolation might greatly reduce the error caused by phenological change, particularly in spring and summer when leaf development was very fast. The basic relationship between interpolated LAI and red, NIR and VIs for each image was firstly analyzed by calculating Pearson's correlation coefficients (r) and examining their scatter plots. Then, the multiple stepwise regression was used alternatively to build LAI prediction models in SPSS (http://www-01.ibm.com/software/analytics/spss/) by using input variables of four spectral bands and seven VIs. The regression-LAI for each image was subsequently compared with the results predicted by NARX model.

2.4. The NARX neural network

The NARX is a recurrent dynamic network, with feedback connections enclosing several layers of the network. The NARX model has been demonstrated to be well suited for modeling nonlinear systems, especially time series (Beale et al., 2011). Moreover, some important qualities of the NARX have also been reported, such as its more effective learning process, faster convergence and better generalization than other neural networks (Diaconescu, 2008; Lin et al., 1996). The NARX model can be expressed in Eq. (11) (Chai et al., 2012; Siegelmann et al., 1997)

$$y(t) = f(y(t-1), y(t-2), \ldots, y(t-i), u(t), u(t-1), u(t-2), \ldots u(t-j)) \tag{11}$$

where the next value of the dependent output signal $y(t)$ is regressed on the previous of the output signal, i.e. $y(t-1), \ldots, y(t-i)$, and the current and previous value of an exogenous input signal, i.e. $u(t), u(t-1), \ldots, u(t-j)$. The i and j are the input and output order, and f is a nonlinear function. The architecture of NARX model is shown in Fig. 2 (Chai et al., 2012). The left two rectangles colored dark gray is tapped delay line (TDL). The input signals enter the TDL and pass through $N-1$ delays. The output of the TDL is an N-dimensional vector made up of the current and previous input signals. The number of delays in the TDL for the input variable u is j and for the output variable y is i.

The data structures of both u and y for the NARX model are in the form of a continuous time-series sequence as shown in Eq. (12) (Chai et al., 2012).

$$\begin{cases} u = \{[u_1] \quad [u_2] \quad \cdots \quad [u_t]\} \\ y = \{[y_1] \quad [y_2] \quad \cdots \quad [y_t]\} \end{cases} \tag{12}$$

where the elements of u and y, i.e. $[u_k]$ and $[y_k]$, respectively, are the values collected at a given time point k ($1 \leqslant k \leqslant t$). By configuring the TDL in advance such as fixing the value of i and j in Eq. (11) with

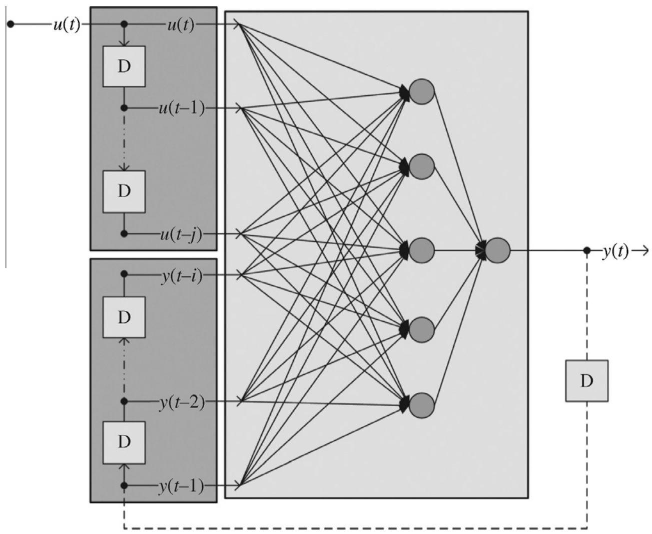

Fig. 2. Architecture of the NARX configured with TDLs.

the input data, the NARX model can be established for time-serials forecasting.

2.4.1. Constructing potential model-building data sets

Since the LAI is changed with seasons, the DOY, together with the four spectral bands and seven VIs were considered as potential exogenous inputs (u), and the interpolated field LAI for each image was the outputs (y). There are 24 model-building stands and 13 successive HJ-1A/1B CCD images. Therefore, the potential exogenous inputs $[u_k]$ and outputs $[y_k]$ in Eq. (12) are of the forms of Eq. (13).

$$\begin{cases} [u_k] = \begin{bmatrix} \mathrm{DOY}_{k1} & \mathrm{DOY}_{k2} & \cdots & \mathrm{DOY}_{kn} \\ B1_{k1} & B1_{k2} & \cdots & B1_{kn} \\ \vdots & \vdots & \vdots & \vdots \\ \mathrm{EVI}_{k1} & \mathrm{EVI}_{k2} & \cdots & \mathrm{EVI}_{kn} \end{bmatrix} \\ [y_k] = [\mathrm{LAI}_{k1} \quad \mathrm{LAI}_{k2} \quad \cdots \quad \mathrm{LAI}_{kn}] \end{cases} \tag{13}$$

where k $(1 \leqslant k \leqslant 13)$ is the given time point, n is the sampling stands set at 24.

2.4.2. Determination of input variables

Some redundant variables should be removed before entering the final model since there are 12 potential exogenous input variables. Determinate the inputs of an ANN model is always a difficult work, here we select variables based on performance testing. Every possible variable combination from the $[u_k]$ by gradually adding input variables was used to build NARX testing models. In addition to fixing the neurons of hidden layers at 10, the training parameters of the testing model were same as those of the final model described in Section 2.4.3. Each testing model was trained for 50 times, and the correlation coefficients (r) between the observed and predicted LAI and *RMSE* for each training were recorded. The mean value of r and *RMSE*, standard deviation, minimum and maximum value of *RMSE* for each testing model were compared. The top two best models with lowest mean *RMSE* or highest mean r for each number of inputs were identified. The adding of variable was stopped when the mean performances of the top two best models increased very slightly. The most promising variable combinations in these best testing models were selected to build the final NARX model. Base on the testing, the DOY, $B1$, $B2$, $B3$, $B4$ and WDVI were selected to build the final NARX model.

2.4.3. Determination of training parameters

The NARX model was built in MATLAB (http://www.mathworks.com). The training data of $[u_k]$ and $[y_k]$ were randomly divided into independent training, validation and testing sets at a ratio of 0.75:0.15:0.15, respectively. The training data set was used to compute the gradient and update the network weights and biases, while the validation data set was used to monitor the error during the training process. After the training process, the test data set error was used to test the training. The training was stopped when the correlation coefficients between each data set and its prediction were consistent. By considering the inaccessibility of the experimental data and the usability and flexibility of the model, the i and j for the TDLs of u and y were both set to 1 (Fig. 2). Therefore, Eq. (11) can be simplified to the form of Eq. (14).

$$y(t) = f(y(t-1), u(t-1), u(t)) \tag{14}$$

where for the mapping function, $y(t)$ was LAI(t) and $u(t)$ was [DOY(t); $B1(t)$; $B2(t)$; $B3(t)$; $B4(t)$; WDVI(t)].

The NARX model was set to a two-layered architecture. Before entering the network, the inputs were standardized and a sigmoidal transformation function was used to calculate the activation of each hidden neuron. In the hidden layer, 13 neurons were used based on performance testing of adding neurons. In order to improve the training speed, the Levenberg–Marquardt backpropagation algorithm was adopted in the training (Beale et al., 2011).

Based on Eq. (14), the exact map of LAI($t-1$), which is always unknown in advance, is needed when mapping LAI(t) over large area with the NARX model. In our study, the LAI($t-1$) over the study area for the first image on 23/03 (hereinafter referred as LAI(0323)) was determined by the best regression results from HJ-1A CCD and ZY-3 MUX images. The 5.8 m ZY3 regression-based LAI was resampled into 30 m spatial resolution by the nearest neighbor methods. However, the estimation errors on LAI(0323) would be augmented and propagated when it was used to predict LAI(t) with the well-trained NARX model, which was built based on accurate field LAI. This problem was particularly more serious when the prediction accuracy of LAI(0323) was low. Therefore, an auxiliary testing criterion was used to find a strong error-tolerant NARX model during the training process. The testing was carried in three steps: (1) using best regression-based LAI(0323) as inputs to predict LAI of next date (here is 24/04, and referred to this LAI as LAI(0424)) with the training model; (2) extracting LAI of the model-building stands from LAI(0424); (3) calculating correlation coefficients and *RMSE* of the predicted LAI with field LAI. The NARX model that possessed the best training performance and its prediction results corresponded well with LAI(0424) was finally selected.

2.4.4. Model performance evaluation

Direct validation and model comparison were conducted to evaluate the performance of the NARX model. The field data of the six validation stands, which began their measurement in August 2012, were used to validate the model. The DOY, $B1$, $B2$, $B3$, $B4$ and WDVI of the model-validation stands from the images of 04/10, 13/10, 22/11 and 01/12 were used to construct $[u_k]$. The interpolated field LAIs of the four images were used to build $[y_k]$. The model comparison was performed by respectively comparing the NARX-based LAI of all the sampling stands with the corresponding stepwise regression-based LAI. The same method described in Section 2.3.4 was used to extract the regression- and NARX-based LAI of each stand from the prediction maps. The scatter plots, coefficient of determination (R^2) of the observed LAI against predicted LAI and *RMSEs* were used to evaluate model performance and to find areas of poorer prediction.

2.4.5. Temporal LAI mapping

In a previous study, we derived a high precision map of rubber plantation (30 m spatial resolution) over Danzhou region by integration of Phased Array type L-band Synthetic Aperture Radar (PALSAR) with multi-temporal Landsat imagery (Dong et al., 2013). An area of 512 $\times$ 512 pixels centered on CATAS experimental farm from this map was used for temporal LAI mapping. During the mapping, the NARX output LAI(t) was used as input parameter to predict the LAI of next date. Based on our measurement, the LAI of rubber plantation is unlikely less than 0.5 and greater than 7, therefore pixel value outside (0.5, 7) were strictly removed. In addition, pixels with LAI value below 2th percentile and above 98th percentile were masked out to eliminate errors that were caused by misclassification and the model itself. Statistics analysis was conducted on each spatio-temporal LAI map and the descriptive results compared with the statistics data of the field LAI.

3. Results

3.1. The temporal variation of field-LAI

The lowest LAI was found in late February with a mean value of 1.18 ± 0.69 (Fig. 3). A quick increase of LAI was observed in March and April, reaching the mean values of 2.17 ± 0.63 and 2.96 ± 0.74, respectively. However, in May, the rising of LAI slowed down but still increased until it reached the maximum value of 4.02 ± 1.05 in late September. A slight decline of mean LAI was found in October (0.07), and a more obvious decrease was observed during November (0.29), December (0.26) and January (0.26). The dramatic fall of LAI was found in February, from 3.14 ± 0.88 to 1.18 ± 0.69, faster than the foliation speed observed in March or April. The standard deviation of LAI ranged from 0.63 to 1.05 during the year.

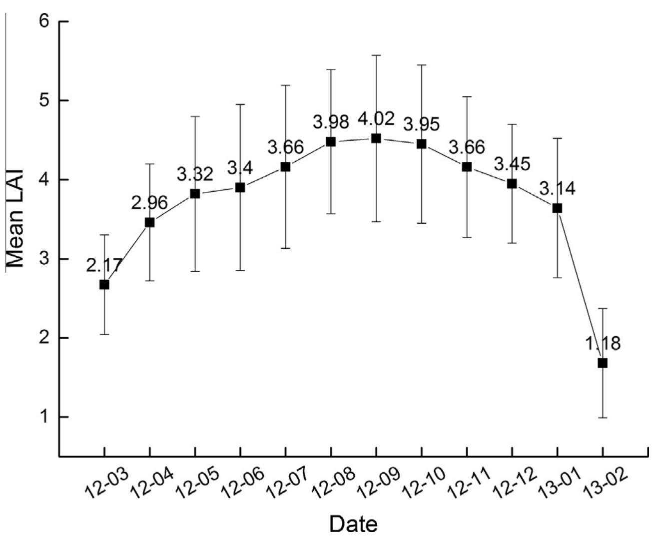

Fig. 3. The temporal variation of mean LAI of the model-building stands at the CATAS experimental farm, Hainan Island, China. The error bars is the standard deviation.

3.2. LAI versus spectral bands and VIs of HJ-1A/1B CCD and ZY3 images

The Pearson's correlation coefficients (r) between the LAI and red, NIR and VIs of the 13 successive HJ-1A/1B CCD and the ZY3 images were presented in Table 4. The red band ($B3$) showed negative correlation with LAI (r = 0.49–0.56) before early May and tended to show very weak correlation since then. Good correlation relationships were observed between the LAI and NIR reflectance ($B4$) and the seven VIs for all the images. However, great difference in correlation strength was found among these variables. The NIR, WDVI, SAVI and TSAVI were highly correlated with field LAI with r ranging from 0.51 to 0.80 for all the images. The NDVI, SR, SAVI2 and EVI showed close relationship with LAI before October but weak correlation relationship with r around 0.45 ($P < 0.05$) since then. The absolute values of correlation coefficients of NIR and VIs for ZY3 were ranged from 0.71 to 0.74, slightly better than those of the HJ-1B CCD images on 23/03.

The scatter plots of predicted LAI versus observed LAI for the model-building stands on 23/03 by stepwise regression from HJ-1B CCD and ZY3 MUX images were presented in Fig. 4. Moderate accuracy prediction results were found for the two images, with R^2 of 0.57 and 0.54 and *RMSEs* of 0.43 and 0.41 for HJ-1B CCD and ZY3 MUX image, respectively. In addition, underestimation of LAI greater than 2.5 was observed for both the two images. The LAI from HJ image was slightly better than results from ZY3 image, and therefore was used as input for both model training and LAI mapping.

3.3. The training results of the NARX model

Fig. 5 shows the regression plots of the NARX output with respect to model-building, validation and testing data and error histogram. The performance of the model during the training was fairly good, reaching R^2 of 0.98, 0.93 and 0.87 and *RMSEs* of 0.13, 0.24, and 0.31 for the data sets of training ($N = 202$),

Table 4
Pearson's correlation coefficients between LAI and red and NIR spectral band, and vegetation indices derived from the 13 successive HJ-1A/1B CCD and one ZY3 images.

No.	Satellite	Sensor	Date	$B3$	$B4$	NDVI	SR	SAVI	SAVI2	TSAVI	WDVI	EVI
1	HJ-1B	CCD2	23/03	−0.51*	0.75**	0.67**	0.68**	0.71**	0.66**	0.67**	0.70**	0.69**
2	ZY3	MUX	23/03	−0.55**	0.74**	0.71**	0.71**	0.71**	0.71**	0.71**	0.74**	−0.71**
3	HJ-1A	CCD1	24/04	−0.49*	0.62**	0.63**	0.63**	0.65**	0.64**	0.65**	0.64**	0.63**
4	HJ-1A	CCD2	01/05	−0.56**	0.68**	0.63**	0.64**	0.66**	0.64**	0.65**	0.67**	0.65**
5	HJ-1B	CCD2	03/05	−0.51*	0.71**	0.66**	0.68**	0.71**	0.69**	0.69**	0.72**	0.69**
6	HJ-1A	CCD1	09/05	−0.34	0.60**	0.52**	0.52**	0.58**	0.56**	0.57**	0.60**	0.57**
7	HJ-1B	CCD2	14/05	−0.37	0.63**	0.51**	0.53**	0.58**	0.53**	0.54**	0.59**	0.57**
8	HJ-1A	CCD2	11/07	−0.28	0.67**	0.56**	0.60**	0.66**	0.60**	0.63**	0.67**	0.60**
9	HJ-1B	CCD2	13/07	−0.10	0.64**	0.49*	0.54**	0.60**	0.56**	0.57**	0.62**	0.57**
10	HJ-1A	CCD2	15/07	−0.28	0.64**	0.60**	0.63**	0.64**	0.63**	0.63**	0.65**	0.62**
11	HJ-1B	CCD1	04/10	0.16	0.61**	0.43*	0.46*	0.55**	0.47**	0.51**	0.57**	0.43*
12	HJ-1A	CCD2	13/10	0.26	0.80**	0.47**	0.49**	0.66**	0.45*	0.54**	0.69**	0.46**
13	HJ-1B	CCD2	22/11	0.09	0.67**	0.41*	0.45*	0.62**	0.45*	0.57**	0.64**	0.46*
14	HJ-1A	CCD2	01/12	0.24	0.77**	0.40*	0.45*	0.64**	0.45*	0.55**	0.70**	0.49**

* Correlation was significantly different at the 0.05 level (2-tailed).
** Correlation was significantly different at the 0.01 level (2-tailed). Twenty-four stands were used for calculation for images before August and 30 stands were used since then.

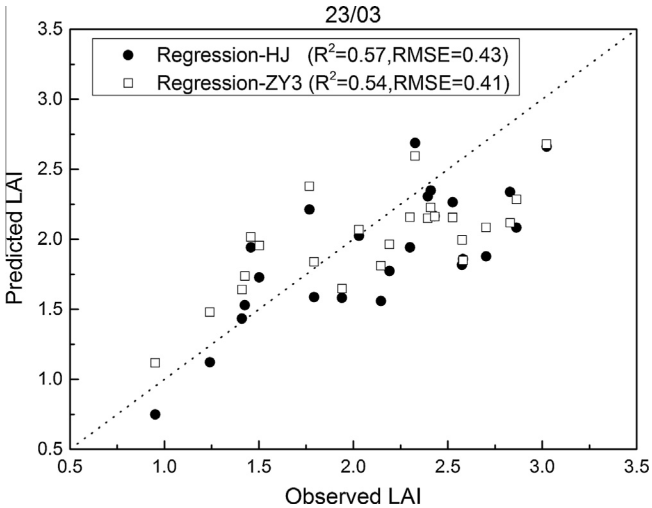

Fig. 4. Scatter plots of LAI on March 23, 2012 predicted by multiple stepwise regression based on HJ-1B CCD and ZY3 MUX images.

validation ($N = 43$) and testing ($N = 43$), respectively. The histogram (Fig. 5d) indicated that the errors were slightly left skewed, but overall were normally distributed. Slight underestimation of high LAI and about six of obvious scatter points were observed during the model validation and test (Fig. 5b and c).

3.4. Performance evaluation of the NARX model

The performance evaluation of NARX model was presented in Fig. 6. Fig. 6a was the scatter plot of the predicted LAI versus observed LAI from the model-validation stands on 13/10, 22/11 and 01/12. The predicted LAI agreed well with the field measurement and reached R^2 and *RMSEs* of 0.88 and 0.24, respectively. However, slight overestimation was observed for about half of the model-validation stands.

The comparison of the NARX predicted LAI with the results from the stepwise regression for image of 03/05, 15/07, 04/10, 13/10 and 22/11 for all the sampling stands were presented in Fig. 6b–f, respectively. The images of 03/05 and 15/07 were selected because they possessed stronger correlation relationship with field LAI in May and July, while the later three images (04/10, 13/10 and 22/11) showed the weakest correlation relationship with the field LAI among these images (Table 4). Before 13/10, the NARX-based LAI presented good consistence with the observed LAI than the correspond regression-based LAI. The R^2 and *RMSE* were ranging from 0.54 to 0.58 and 0.47 to 0.71, and 0.43 to 0.51 and 0.52 to 0.82 for the NARX models and regression models, respectively. However, the results after 13/10 were unexpected, which the regression models obviously showed better performance than the NARX models. The R^2 and *RMSE* of the regression models were 0.56 and 0.66, and 0.56 and 0.56 for image of 22/11 and 01/12, respectively. The NARX models, however, held lower R^2 of 0.23 and 0.39 and *RMSE* of 0.71 and 1.01 for the two days, respectively.

3.5. Model input testing

Since the LAI predictions from multivariate regression models after 13/10 were obviously better than the NARX model (Fig. 6e and f), an input testing for the NARX model was carried out to explore some potential factors which affects the model prediction accuracy. The regression-based LAI and NARX-based LAI on 13/10 was respectively used as LAI($t - 1$) to predict LAI of 22/11 and

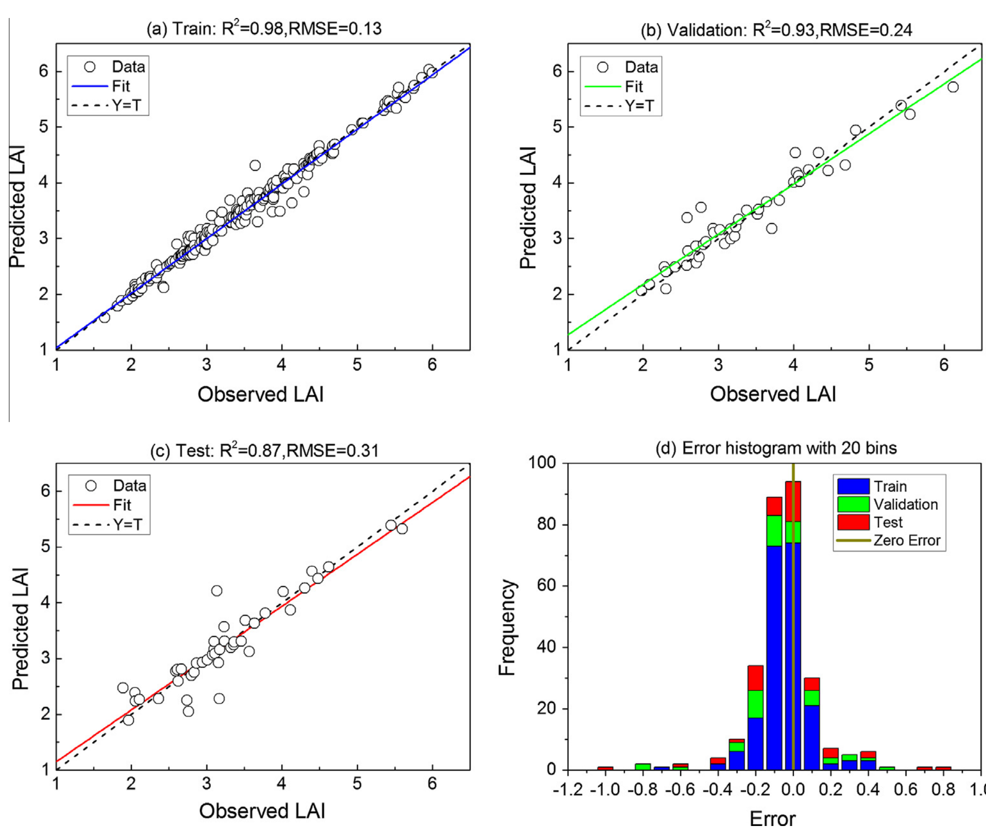

Fig. 5. Regression plots of the NARX model for the output with respect to (a) model building, (b) validation, (c) testing data and error histogram (d). The solid line is the regression line and the dashed line is the one-to-one line.

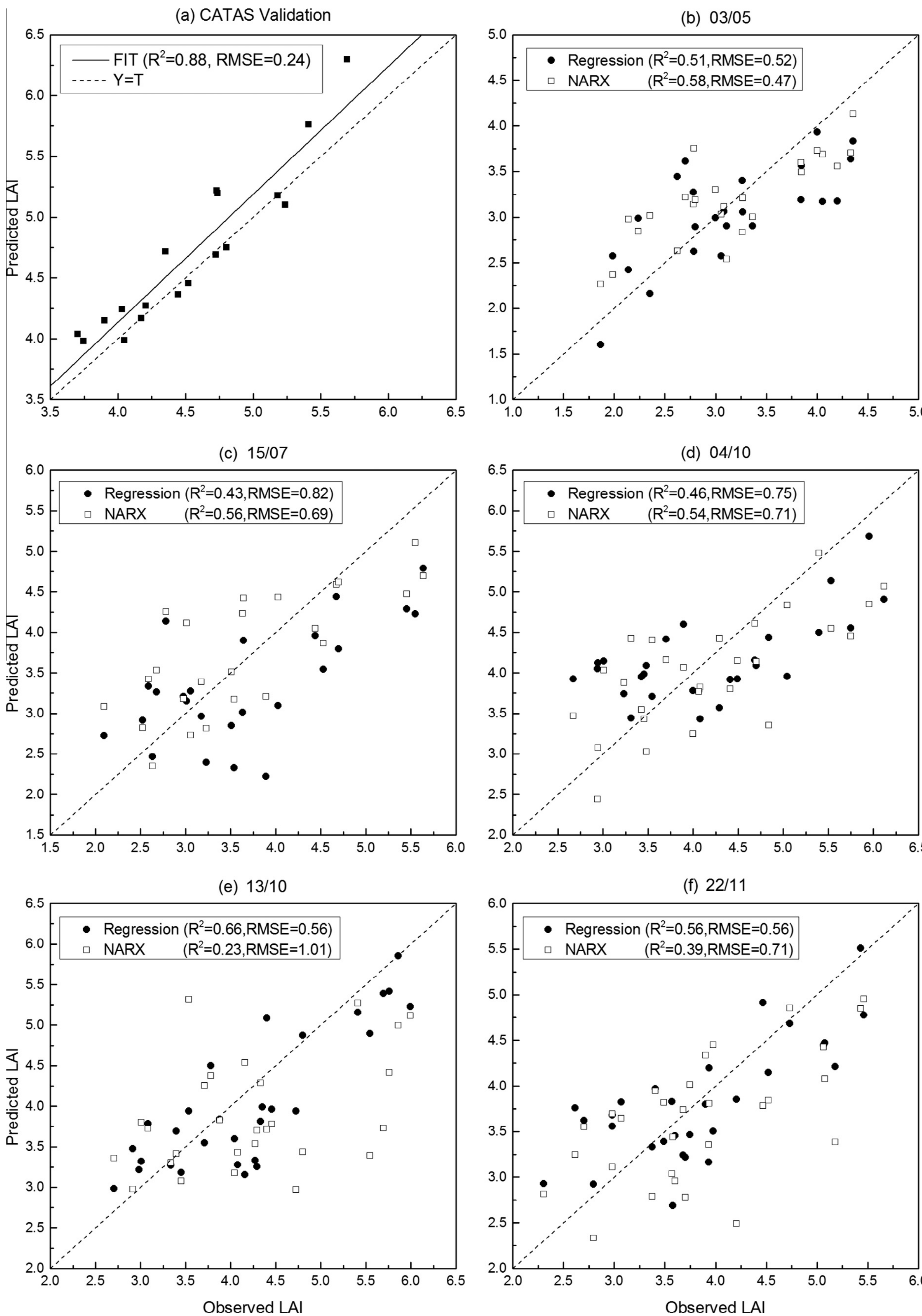

Fig. 6. NARX model performance evaluation: validate with CATAS field data (a) and compared with results from stepwise regression model for image 03/05 (b), 15/07 (c), 04/10 (d), 13/10 (e) and 22/11 (f), respectively.

01/12, and their predicted results were presented in Fig. 7. The LAI from regression-based inputs were compact and less biased along the one-to-one line. The R^2 and *RMSE* were 0.73 and 0.73, and 0.43 and 0.45 for the images 22/11 and 01/12, respectively. The NARX-based output was biased on 22/11 but more scattered and biased on 01/12, the R^2 were 0.39 and 0.28, and *RMSE* were 0.71 and 0.98, respectively.

3.6. Temporal LAI of rubber plantation over CATAS experimental farm

Fig. 8 presents the spatio-temporal LAI maps of rubber plantations over the CATAS area predicted by multiple stepwise regression and the NARX model. The data in brackets were the contemporary statistics results from model-building stands observed in the CATAS experimental farm. On 23/03, both the LAI value and its spatial variation were small, having mean, minimum and maximum values of 2.36 ± 0.59, 0.97 and 3.74, respectively. In May, the mean LAI significantly increased, and reached its mean value of 3.22 ± 0.64. An obvious increase of mean LAI and standard deviation was observed on 15/07 (3.96 ± 0.91). Both the mean and standard deviation of LAI reached their peak value on 04/10, having mean and maximum values of 4.21 ± 0.87 and 6.58, respectively. Later, the mean LAI began to decline and decreased to 3.96 ± 0.84 on 22/11. The mean, standard deviation and maximum LAI derived from the prediction maps shared the same variation trend with the data observed in the CATAS experimental farm.

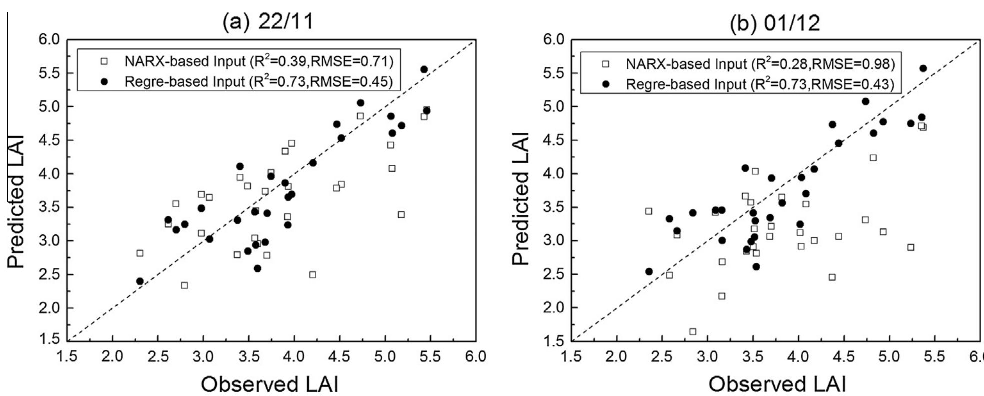

Fig. 7. Comparison of NARX output for images on 22/11 (a) and 01/12 (b) by respectively using NARX-based LAI and Regression-based LAI of 13/10 as model inputs.

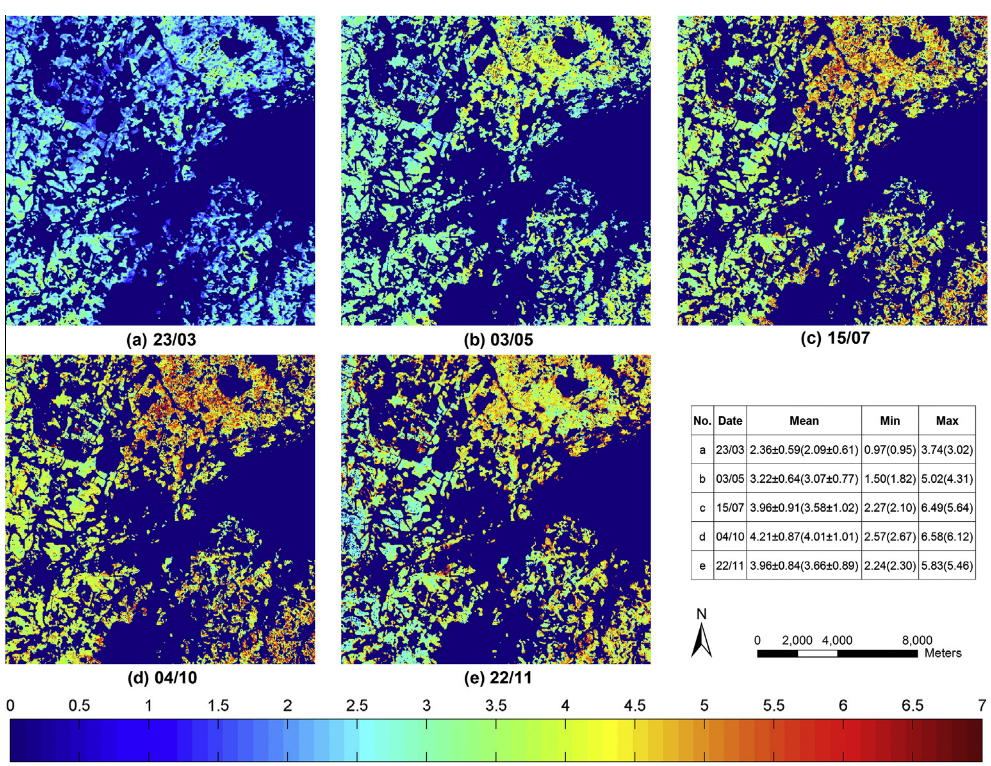

No.	Date	Mean	Min	Max
a	23/03	2.36±0.59(2.09±0.61)	0.97(0.95)	3.74(3.02)
b	03/05	3.22±0.64(3.07±0.77)	1.50(1.82)	5.02(4.31)
c	15/07	3.96±0.91(3.58±1.02)	2.27(2.10)	6.49(5.64)
d	04/10	4.21±0.87(4.01±1.01)	2.57(2.67)	6.58(6.12)
e	22/11	3.96±0.84(3.66±0.89)	2.24(2.30)	5.83(5.46)

Fig. 8. Spatio-temporal LAI maps of rubber plantation over CATAS area (512 × 512 pixels, 30 m spatial resolution) predicted by multiple stepwise regression and the NARX model with HJ-1A/1B CCD images. The LAI on 23/03 (a) was predicted by stepwise regression and 03/05 (b), 15/07 (c), 04/10 (d) and 22/11 (e) were predicted by the NARX model. The non-rubber pixels have been masked out. The descriptive statistics data in brackets was derived from field data of the model-building stands at CATAS experimental farm.

4. Discussion

4.1. General pattern of temporal LAI of rubber plantations in Hainan Island

The temporal variation of LAI (Fig. 3) was quite consistent with the phenological change of rubber trees in Hainan Island. The lowest LAI was observed in February (1.18 ± 0.69) mainly because most rubber trees had shed their leaves. Rubber trees present deciduous behavior with almost complete defoliation for about 2–3 weeks during wintertime, usually in February in Hainan Island, due mainly to the decrease in air temperature and to annual drought (Dong et al., 2013; Righi and Bernardes, 2008). They begin their defoliation when the rainy season ends in October, but most of the leaves are shed during February. Generally, the progress of defoliation is closely related to stand age, but it also depends on site conditions, such as the supply of nutrients, water, or others. The standard deviation of LAI increased in the rainy season is mainly because the young trees usually have more nutrients for canopy development, while mid-age and old trees need more nutrients for latex reproduction and therefore have slower speed of canopy development.

The rubber trees in Hainan Island usually have three distinct foliation periods, in March, May and August, of which the first two periods develop about 80% of the total annual leaves (He and Huang, 1987). If the lowest LAI in February is taken as a benchmark regardless of a few leaves still on the trees, the mean LAI by the end of June (3.40) accounts for 78.17% of the annual maximum LAI (4.02). This proportion is quite consistent with the results reported by He and Huang (1987).

The change of LAI from October to January, however, did not follow a trend of gradual decrease as expected. The mean decrement of LAI during November (0.29) was obviously greater than that in October (0.07) and slightly larger than that in December (0.26) and in January (0.26). This was mainly caused by the disturbance of the strong and late-forming typhoon Son-Tinh, which entered the South China Sea and affected Vietnam and Hainan Island during 26–31th of October 2012, a little later than the field measurements that were made during 21–24th of the same month. Although the Son-Tinh did not directly hit Hainan Island, the continuous stormy weather blew off many rubber leaves. This also indicated that, in terms of post-hurricane damage evaluation, it was of vital importance to intensively monitor the LAI of rubber plantations.

4.2. Relationship between LAI and spectral bands and VIs

Compared with the seven VIs, the NIR showed the strongest correlation relationship with LAI for all the HJ-1A/1B CCD images (Table 4). In addition to explained by the strong reflection of healthy green vegetation in NIR spectral band, the relative strong energy in NIR for the HJ-1A/1B CCD image might also contribute to the high correlation relationship. The WDVI, SAVI and TSAVI, which have incorporated soil line parameters or adjusted factors during calculation, had successfully eliminated both atmosphere and canopy background variation to some degree, and therefore were highly correlated with LAI (Liang and Liang, 2003). Although the ZY3 MUX possessed high image quality than HJ-1A/1B CCD, its correlation coefficients of LAI-NIR and LAI-VIs were slightly better than those of the CCD images. In addition, no significant difference between the regression-LAI for the two images was found. This might be by explained by the fact that the average LAI was very low in March. Therefore, the influence of understory vegetation weakened their correlation strength. Generally, the strong correlation relationship between LAI and spectral bands and VIs throughout the year indicated that it was possible to predict the LAI of rubber plantation by using some of the image-based variables.

4.3. Spatio-temporal LAI of rubber plantation predicted by NARX model

The NARX model developed by the field data of model-building stands and 13 successive HJ-1A/1B CCD images was performed very well. All the R^2 of the predicted LAI versus observed LAI during model training were greater than 0.87, and *RMSEs* were less than 0.31. However, about six of obvious scatter points were found during model building (Fig. 5b and c). A carefully checking of the data indicated that two of them were derived from field measurement error, and four were from model prediction error. The slight underestimation for higher LAI (Fig. 5b and c) might be explained by the decrease in reflectance response of overstory in the closed rubber stands.

The validation of the model with the field data was performed very well ($R^2 = 0.88$, $RMSE = 0.24$). However, unlike the results of the training, no underestimation for lower LAI but slight overestimation of few stands was observed. This was mainly caused by the obvious drop of mean LAI (0.29) after the typhoon Son-Tinh in late October, while the model output was based on assumption that LAI was nonlinear continuous time series. The comparison results in Fig. 6(b–d) also indicated that NARX model was more stable and robust than the corresponding stepwise regression models. However, the results after 13/10 were quite unexpected because the regression-LAI obvious better than NARX-LAI. By carefully checking, we found the image on 13/10 was slightly blurred and possessed significant higher value of red band reflectance than the image of 04/10 and 22/11. The red reflectance should be relatively low since the canopy of rubber plantation was very dense in October. Therefore, we suspect there was a uniform layer of mist over the study area and finally led to a high value of red reflectance. However, a significant high correlation relationship between LAI and NIR ($r = 0.80$) was found under the unique weather (Table 4). The better performance of regression-LAI on 13/10 indicated it was more suitable for LAI mapping and finally was used to predict the LAI of 22/11 and 01/12 with NARX model.

The application of the model over the CATAS area indicated that the predicted results agreed well with the phenological change of rubber trees (Fig. 8). The mean, standard deviation and maximum value of LAI derived from the spatio-temporal LAI maps were consistent with the statistical results of the corresponding field data observed in the CATAS experimental farm. However, there were still some inconsistent spatial variations for few stands on these maps due to failed to obtain a highly accurate LAI map on 23/03. Generally, the NARX model was seem to provide accurate estimates of LAI of rubber plantation throughout the growing season, and it was believed that this approach could be applied to a large area for regional LAI mapping.

4.4. Uncertainty analysis and application prospect

Although majority of the predicted LAI from NARX model (before 13/10) performed reasonable good performance, none of them was significantly better than the corresponding regression-LAI (i.e., Fig. 6b–d). We suspected that the main reason for this was lack of accurate LAI map on 23/03 as model input during the LAI mapping. Neither of the regression results from HJ-1B CCD or ZY3 MUX were very satisfactory since the maximum R^2 was 0.57 and the best *RMSE* was 0.41 (Fig. 4). We also have tried to build a more accurate and robust NN-LAI model on 23/03, but failed because there was only 24 field data available. However, the NARX-LAI on 22/11 and 01/12 were greatly improved when a more accurate regression-LAI map on 13/10 was used (Fig. 7). The R^2 for the two days was greater than 0.73, and the *RMSE* was less than 0.45, far better than the results based on previous NARX output LAI as model input. The input parameter testing indicated that it was a vital step to improve the accuracy of LAI map for the first image (LAI($t-1$)) in spatio-temporal LAI mapping by NARX model. By doing this, we suggest to collect a large number of samples during the first field campaign or to apply multi-source satellite data to improve the overall LAI prediction accuracy for the first image.

In addition, special care should be taken when the NARX model is applied to predict LAI of an area that suffers severe nature disasters because the model is built mainly on the basis that the LAI was nonlinear continuous times series. Slight overestimation of LAI was found with CATAS validation data (Fig. 6a) due to the typhoon Son-Tinh in late October, which give us a hint that additional errors might be raised when LAI suddenly dropped due to natural disasters.

The operational utilization of remote sensing techniques for intensively monitoring the structural parameters of certain crops is often constrained by the scarcity of successive high-resolution images. Benefited from high temporal- and spatial-resolution of the HJ-1A/1B CCD images, a high-precision LAI dynamic monitoring NARX model for rubber plantation was successfully established. The temporal resolution of satellite is particularly important in the tropical area frequently covered with thick clouds, which makes it more difficult to obtain cloud-free optical satellite data there (Ricciardelli et al., 2008; Watmough et al., 2011). For example, only one cloud-free ETM+ image was available for the study area during 2012, but more than 10 good HJ-1A/1B CCD images were obtainable. We believe that this approach is suitable for monitoring parameters of different crops in other regions as long as adequate field data and high-accuracy map of that parameter for the first image are available.

5. Conclusions

It is essential to understand the LAI dynamics of rubber plantations and their relationship with satellite images for regional production management, ecosystem process modeling and post-hurricane damage evaluation. In this study, the temporal variation of LAI of rubber plantation and their relationship with 13 successive HJ-1A/1B CCD images were studied, and a NARX model to predict temporal LAI over the area of CATAS Experimental Farm was developed. The specific conclusions were as follows:

The temporal variation of LAI observed in the CATAS experimental farm was quite consistent with the phenological change of rubber trees in Hainan Island. The LAI was lowest in late February (1.18 ± 0.69), but it quickly increased in March and continued to increase until late September (4.02 ± 1.05), and then it began to decline. The LAI developed in the main foliation period (March to June) accounted for 78.17% of the annual maximum LAI.

The NIR, WDVI, SAVI and TSAVI derived from HJ-1A/1B CCD images were highly correlated with LAI for all the images (r = 0.51–0.80, p < 0.01), while the NDVI, SR, SAVI2 and EVI showed close relationship with LAI before October but weak correlation since then. An NARX model was successfully developed by using DOY, four spectral bands, WDVI and previous LAI result as inputs. Very good agreements between the predicted and observed LAI for model building (R^2 > 0.87, *RMSE* < 0.31) and field validation (R^2 = 0.88, *RMSE* = 0.24) were obtained. The application of the model over the area of CATAS Experimental Farm also indicated that the prediction results were quite satisfactory. Before the 13/10, all predictions derived from the NARX model showed better agreements with the field data than the results from corresponding stepwise regression models; despite that the key input parameter of the NARX model was not very accurate in LAI mapping. Besides, the LAI statistical values from the spatio-temporal LAI maps and their dynamics were quite consistent with the statistical results of the field data that observed in the CATAS experimental farm.

In brief, this study demonstrated a great potential in applying HJ-1A/1B CCD images and the NARX model to retrieve the spatio-temporal LAI of rubber plantations in Hainan Island, China. However, obtaining an accurate LAI map in advance, by means such as collecting a large amount of samples during the first field campaign or aiding with multi-source satellite images, was a key step in applying NARX model to monitor the LAI dynamics of rubber plantations or other vegetation.

Acknowledgements

This research was funded in part by Danzhou Investigation & Experiment Station of Tropical Crops, Ministry of Agriculture, P.R. China, and the Earmarked Fund for China Agriculture Research System (CARS-34-GW5), and the Fundamental Research Funds for Rubber Research Institute, CATAS (1630022011012, 1630022012019), and Natural Science Foundation of Hainan Province (314138), and NASA LCLUC Program (NNX14AD78G). Thanks to Prof. Feirong Gu from Nanjing Agricultural University and Prof. Janlan Zhou from RRI, CATAS for their English editing and useful comments. We also would like to thank the several anonymous reviewers whose questions and comments resulted in a much deeper, more complete analysis.

References

Aosier, B., Kaneko, M., Takada, M., 2007. Evaluation of the forest damage by typhoon using remote sensing technique. In: Geoscience and Remote Sensing Symposium, 2007. IGARSS 2007. IEEE International, Barcelona, pp. 3022–3026.

Bacour, C., Baret, F., Béal, D., Weiss, M., Pavageau, K., 2006. Neural network estimation of LAI, fAPAR, fCover and LAIxCab, from top of canopy MERIS reflectance data: principles and validation. Remote Sens. Environ. 105, 313–325.

Beale, M.H., Hagan, M.T., Demuth, H.B., 2011. Neural Network Toolbox User's Guide. MathWorks Inc., Natick, MA. <http://www.mathworks.com/help/pdf_doc/nnet/nnet_ug.pdf>.

Berterretche, M., Hudak, A.T., Cohen, W.B., Maiersperger, T.K., Gower, S.T., Dungan, J., 2005. Comparison of regression and geostatistical methods for mapping leaf area index (LAI) with Landsat ETM+ data over a boreal forest. Remote Sens. Environ. 96, 49–61.

Broge, N.H., Leblanc, E., 2000. Comparing prediction power and stability of broadband and hyperspectral vegetation indices for estimation of green leaf area index and canopy chlorophyll density. Remote Sens. Environ. 76, 156–172.

Chai, L., Qu, Y., Zhang, L., Liang, S., Wang, J., 2012. Estimating time-series leaf area index based on recurrent nonlinear autoregressive neural networks with exogenous inputs. Int. J. Remote Sens. 33, 5712–5731.

Chander, G., Brian, L.M., Dennis, L.H., 2009. Summary of currentradiometriccalibration coefficients for Landsat MSS, TM, ETM+, and EO-1 ALI sensors. Remote Sens. Environ. 113, 893–903.

Chen, J.M., Cihlar, J., 1996. Retrieving leaf area index of boreal conifer forests using Landsat TM images. Remote Sens. Environ. 55, 153–162.

Chen, X., Vierling, L., Rowell, E., DeFelice, T., 2004. Using lidar and effective LAI data to evaluate IKONOS and Landsat 7 ETM+ vegetation cover estimates in a ponderosa pine forest. Remote Sens. Environ. 91, 14–26.

Chen, C., Wang, R., Jiang, J., 2007. Variation of soil fertility and carbon sequestration by planting *hevea brasiliensis* in Hainan Island, China. J. Environ. Sci. 19, 348–352.

Chen, J., Mo, Y., Chen, M., Wei, H., Sun, J., 2010. Potential analyse of natural rubber production in China. Trop. Agric. Eng., 90–98

Chen, X., Meng, J., Du, X., Zhang, F., Zhang, M., Wu, B., 2010. The monitoring of the winter wheat leaf area index based on HJ-1 CCD data. Remote Sens. Land Resour., 55–58

Chen, B., Cao, J., Wang, J., Wu, Z., Tao, Z., Chen, J., Yang, C., Xie, G., 2012. Estimation of rubber stand age in typhoon and chilling injury afflicted area with Landsat TM data: a case study in Hainan Island. China. Forest Ecol. Manage. 274, 222–230.

Diaconescu, E., 2008. The use of NARX neural networks to predict chaotic time series. WSEAS Trans. Comput. Res. 3, 182–191.

Dong, J., Xiao, X., Chen, B., Torbick, N., Jin, C., Zhang, G., Biradar, C., 2013. Mapping deciduous rubber plantations through integration of PALSAR and multi-temporal Landsat imagery. Remote Sens. Environ. 134, 392–402.

Fang, H., Liang, S., 2003. Retrieving leaf area index with a neural network method: simulation and validation. IEEE Trans. Geosci. Remote Sens. 41, 2052–2062.

Fang, H., Liang, S., 2005. A hybrid inversion method for mapping leaf area index from MODIS data: experiments and application to broadleaf and needleleaf canopies. Remote Sens. Environ. 94, 405–424.
Fassnacht, K.S., Gower, S.T., MacKenzie, M.D., Nordheim, E.V., Lillesand, T.M., 1997. Estimating the leaf area index of North Central Wisconsin forests using the landsat thematic mapper. Remote Sens. Environ. 61, 229–245.
Foody, G.M., Cutler, M.E., Mcmorrow, J., Pelz, D., Tangki, H., Boyd, D.S., Douglas, I., 2001. Mapping the biomass of Bornean tropical rain forest from remotely sensed data. Global Ecol. Biogeogr. 10, 379–387.
Fu, F., Zhang, D., 2010. Rubber tree windstorm insurance and its improvement. Trop. Agric. Sci. Technol. 33, 38–42.
González-Sanpedro, M.C., Le Toan, T., Moreno, J., Kergoat, L., Rubio, E., 2008. Seasonal variations of leaf area index of agricultural fields retrieved from Landsat data. Remote Sens. Environ. 112, 810–824.
Gray, J., Song, C., 2012. Mapping leaf area index using spatial, spectral, and temporal information from multiple sensors. Remote Sens. Environ. 119, 173–183.
He, K., Huang, Z., 1987. Rubber Culture in the Northern Part of Tropical Area. Guangdong Science & Technology Press, Guangdong.
Houborg, R., Soegaard, H., Boegh, E., 2007. Combining vegetation index and model inversion methods for the extraction of key vegetation biophysical parameters using Terra and Aqua MODIS reflectance data. Remote Sens. Environ. 106, 39–58.
Hu, Y., Wang, Z., Shu, Y., Wu, Y., 1982. Studies on photosynthesis of hevea population II. A mathematical model for estimating the photosynthetic output of hevea population. Chinese J. Trop. Crops. 3, 41–48.
Hu, Z., Zhiyuan, P., Shangjie, M., Lianlin, W., Zhiping, M., 2012. Retrieving leaf area index of winter wheat using HJ-1-A/B CCD2 data. Trans. Chinese Soc. Agric. Eng. 28, 172–176.
Jensen, J.R., Qiu, F., Ji, M., 1999. Predictive modelling of coniferous forest age using statistical and artificial neural network approaches applied to remote sensor data. Int. J. Remote Sens. 20, 2805–2822.
Jensen, J.L.R., Humes, K.S., Hudak, A.T., Vierling, L.A., Delmelle, E., 2011. Evaluation of the MODIS LAI product using independent lidar-derived LAI: a case study in mixed conifer forest. Remote Sens. Environ. 115, 3625–3639.
Jonckheere, I., Fleck, S., Nackaerts, K., Muys, B., Coppin, P., Weiss, M., Baret, F.D.R., 2004. Review of methods for in situ leaf area index determination: Part I. Theories, sensors and hemispherical photography. Agric. Forest Meteorol. 121, 19–35.
Ju-sheng, J., Ru-song, W., 2003. Hydrological eco-service of rubber plantations in Hainan Island and its effect on local economic development. J. Environ. Sci. 15, 701–709.
le Maire, G., Marsden, C., Verhoef, W., Ponzoni, F.J., Lo Seen, D., Bégué, A., Stape, J., Nouvellon, Y., 2011. Leaf area index estimation with MODIS reflectance time series and model inversion during full rotations of Eucalyptus plantations. Remote Sens. Environ. 115, 586–599.
Li, Z., Fox, J.M., 2011. Integrating Mahalanobis typicalities with a neural network for rubber distribution mapping. Remote Sensing Lett. 2, 157–166.
Li, W., Li, H., Zhao, L., 2011. Estimating rice yield by HJ-1A satellite images. Rice Sci. 18, 142–147.
Liang, S., Liang, S., 2003. Quantitative Remote Sensing of Land Surfaces. Wiley Interscience.
LI-COR, I., 1992. LAI-2000 Plant Canopy Analyzer Operating Manual. LI-COR Inc., Lincoln, NE. <ftp://ftp.licor.com/perm/env/LAI-2000/Manual/LAI-2000_Manual.pdf>.
LI-COR, I., 2012. LAI-2200 Plant Canopy Analyzer Instruction Manual. LI-COR, Inc., Lincoln, NE. <ftp://ftp.licor.com/perm/env/LAI-2200/Manual/LAI-2200_Manual.pdf>.
Lin, T., Horne, B.G., Tino, P., Giles, C.L., 1996. Learning long-term dependencies in NARX recurrent neural networks. IEEE Trans. Neural Networks 7, 1329–1338.
Linna, C., Yonghua, Q., Lixin, Z., Shunlin, L., Jindi, W., 2009. Estimating time series leaf area index based on recurrent neural networks. Adv. Earth Sci. 24, 756–768.
Lu, S., Wu, B., Yan, N., Wang, H., 2011. Water body mapping method with HJ-1A/B satellite imagery. Int. J. Appl. Earth Obs. Geoinf. 13, 428–434.
Maass, J., Vose, J.M., Swank, W.T., Martínez-Yrízar, A., 1995. Seasonal changes of leaf area index (LAI) in a tropical deciduous forest in west Mexico. Forest Ecol. Manage. 74, 171–180.
Menezes Jr., J.M.P., Barreto, G.A., 2008. Long-term time series prediction with the NARX network: an empirical evaluation. Neurocomputing 71, 3335–3343.
Mo, Y., 2010. Production and marketing of nature rubber in 2009 and market forecast in 2010. China Trop. Agric., 12–15
Murnion, Shane D., 1996. Comparison of back propagation and binary diamond neural networks in the classification of a Landsat TM image. Comput. Geosci. 22, 995–1001.
Muukkonen, P., Heiskanen, J., 2005. Estimating biomass for boreal forests using ASTER satellite data combined with standwise forest inventory data. Remote Sens. Environ. 99, 434–447.
Olthof, I., King, D.J., 2000. Development of a forest health index using multispectral airborne digital camera imagery. Can. J. Remote Sens., 166–176
Pisoni, E., Farina, M., Carnevale, C., Piroddi, L., 2009. Forecasting peak air pollution levels using NARX models. Eng. Appl. Artif. Intel. 22, 593–602.
Ricciardelli, E., Romano, F., Cuomo, V., 2008. Physical and statistical approaches for cloud identification using meteosat second generation-spinning enhanced visible and infrared imager data. Remote Sens. Environ. 112, 2741–2760.
Righi, C., Bernardes, M., 2008. The potential for increasing rubber production by matching tapping intensity to leaf area index. Agroforest. Syst. 72, 1–13.
Sauter, T., Weitzenkamp, B., Schneider, C., 2010. Spatio-temporal prediction of snow cover in the Black Forest mountain range using remote sensing and a recurrent neural network. Int. J. Climatol. 30, 2330–2341.
Shupe, S.M., Marsh, S.E., 2004. Cover- and density-based vegetation classifications of the Sonoran Desert using Landsat TM and ERS-1 SAR imagery. Remote Sens. Environ. 93, 131–149.
Siegelmann, H.T., Horne, B.G., Giles, C.L., 1997. Computational capabilities of recurrent NARX neural networks. IEEE Trans. Syst. Man Cybern. B Cybern. 27, 208–215.
Soudani, K., François, C., le Maire, G., Le Dantec, V., Dufrêne, E., 2006. Comparative analysis of IKONOS, SPOT, and ETM+ data for leaf area index estimation in temperate coniferous and deciduous forest stands. Remote Sens. Environ. 102, 161–175.
Sprintsin, M., Cohen, S., Maseyk, K., Rotenberg, E., Grünzweig, J., Karnieli, A., Berliner, P., Yakir, D., 2011. Long term and seasonal courses of leaf area index in a semi-arid forest plantation. Agric. Forest Meteorol. 151, 565–574.
Sun, Y., Gu, X., Yu, T., Gao, H., Li, J., Hu, X., 2011. Research on the inversion of leaf area index based on radiative transfer model of HJ-1A CCD data. J. Anhui Agric. Sci. 39, 5012–5015.
Tian, Q., Luo, Z., Chen, J.M., Chen, M., Hui, F., 2007. Retrieving leaf area index for coniferous forest in Xingguo County, China with Landsat ETM+ images. J. Environ. Manage. 85, 624–627.
Turner, D.P., Cohen, W.B., Kennedy, R.E., Fassnacht, K.S., Briggs, J.M., 1999. Relationships between leaf area index and landsat TM spectral vegetation indices across three temperate zone sites. Remote Sens. Environ. 70, 52–68.
Walthall, C., Dulaney, W., Anderson, M., Norman, J., Fang, H., Liang, S., 2004. A comparison of empirical and neural network approaches for estimating corn and soybean leaf area index from Landsat ETM+ imagery. Remote Sens. Environ. 92, 465–474.
Wang, B., Ono, A., Muramatsu, K., Fujiwara, N., 1999. Automated detection and removal of clouds and their shadows from Landsat TM images. IEICE Trans. Inform. Syst. E82, 453–460.
Watmough, G.R., Atkinson, P.M., Hutton, C.W., 2011. A combined spectral and object-based approach to transparent cloud removal in an operational setting for Landsat ETM+. Int. J. Appl. Earth Obs. Geoinf. 13, 220–227.
Welles, J.M., Norman, J.M., 1991. Instrument for indirect measurement of canopy architecture. Agron. J. 83, 818–825.
Xie, G., 2009. Modeling of Photosynthesis and Dry Matter Accumulation of Rubber Tree and Analysis of the Potential for Rubber Production in Hainan Province. China Agricultural University, Beijing.
Xie, G., Chen, B., Wang, J., Wu, Z., Huang, Y., 2010. Studies on the simulation model of photosynthesis and dry matter accumulation for rubber tree. Chinese Agric. Sci. Bull. 26, 317–323.
Yu, W., Zhang, M., Mai, Q., Jiang, J., 2006. Damage of Typhoon Damrey to the rubber industry in Hainan state farm bureau and its countermeasures for future development. Chinese J. Trop. Agric. 26, 41–43.
Zhang, D., 2011. Study on practice of rubber tree windstorm insurance in Hainan state farms. Issues Forest. Econ. 31, 145–148.
Zhang, J., Gu, X., Wang, J., Huang, W., Xin, H., Wang, H., 2010. Analysis of consistency between HJ-CCD images and TM images in monitoring rice LAI. Trans. CSAE 26, 186–193.
Zhang, K., Song, C., Chen, Y., 2010. Records and disaster assessment of typhoons in East Hainan Island in recent 50 years. J. Anhui Agric. Sci. 38, 12880–12882.
Zhang, Y., Meng, Q., Wu, J., Zhao, F., 2011. Study of environmental vegetation index based on environmental satellite CCD data and LAI inversion. Spectrosc. Spectral Anal. 31, 2789–2793.
Zheng, G., Moskal, L.M., 2009. Retrieving leaf area index (LAI) using remote sensing: theories methods and sensors. Sensors, 2719–2745.
Zhu, G., Li, M., Ju, W., Chen, J., Wu, Z., 2011. Difference in leaf area index in forests retrieved from HJ-1 CCD and TM data of Maoershan mountain, Heilongjiang province. J. Northeast Forest. Univ. 39, 127–130.